applied sciences

MDPI

Article

Potential of Fluid Dynamic Bowtie Filter for Dose Reduction and Image Quality Improvement of Cone-Beam CT

Xin Lin, Weihai Zhuo *, Haikuan Liu and Tianwu Xie

Institute of Radiation Medicine, Fudan University, 2094 Xietu Road, Shanghai 200032, China
* Correspondence: whzhuo@fudan.edu.cn; Tel./Fax: +86-021-6643-3568

Abstract: Reducing radiation dose to patients without compromising imaging quality has been an important issue in the medical use of X-ray computed tomography (CT). In this study, based on the conceptual designs of different types of attenuation filters, the radiation doses to patients who undergo a typical head, thorax and abdomen scan using a cone-beam CT with different scanning protocols were simulated using the Monte Carlo method, and the isotropy of the noise power spectrum (NPS) of the reconstructed images was also calculated. Compared to the scanning protocol without attenuation and tube current modulation (TCM), the results showed that the fluid dynamic bowtie filter (FDB) combined with the TCM technique reduced the average organ dose by 70%, 34% and 60% for a typical head, thorax and abdomen scan, respectively, and the NPS isotropy of the reconstructed images was also significantly improved. Compared to most currently used static bowtie filters, the FDB has a higher potential to reduce the dose for patients undergoing CT scans. Further efforts are warranted to make the FDB technique clinically useful.

Keywords: CT; fluid dynamic bowtie filter; static bowtie filter; radiation dose; NPS isotropy

check for updates

Citation: Lin, X.; Zhuo, W.; Liu, H.; Xie, T. Potential of Fluid Dynamic Bowtie Filter for Dose Reduction and Image Quality Improvement of Cone-Beam CT. *Appl. Sci.* **2022**, *12*, 9346. https://doi.org/10.3390/app12189346

Academic Editor: Marco Giannelli

Received: 11 August 2022
Accepted: 16 September 2022
Published: 18 September 2022

Publisher's Note: MDPI stays neutral with regard to jurisdictional claims in published maps and institutional affiliations.

Copyright: © 2022 by the authors. Licensee MDPI, Basel, Switzerland. This article is an open access article distributed under the terms and conditions of the Creative Commons Attribution (CC BY) license (https://creativecommons.org/licenses/by/4.0/).

1. Introduction

X-ray computed tomography (CT) is widely used in clinical practices. CT images can be used for disease diagnosis, for the guidance of interventional procedures or radiotherapy, as well as for tumor and normal tissue localization before radiotherapy. According to the latest report of the United Nations Scientific Committee on the Effect of Atomic Radiation (UNSCEAR), although CT accounts for only approximately 10% of all X-ray diagnostic procedures, it makes the largest contribution (61.6%) to the collective effective dose [1]. In recent years, several studies have quantified the non-ignorable cancer risk associated with the use of diagnostic CT, especially for children [2–4]. Therefore, reducing the dose for patients undergoing medical CT examinations has been widely studied.

To reduce the potential health risks of CT examinations, many techniques have been developed in the past decades and proven to be efficient in reducing the radiation dose delivered to patients without compromising image quality. Serval techniques, such as automatic exposure control (AEC) [5], tube current modulation (TCM) [6–9] and spatial filtration [10], have been widely used. Moreover, the pre-patient attenuator with the shape of a hat called a "bowtie filter" or "bowtie" has been practically adopted in most newly developed CT scanners. A bowtie filter can selectively attenuate photons emitted from the X-ray tube as a function of the angle of the X-ray. In addition, by blocking radiation to the periphery of a patient where the attenuation path is the shortest, the radiation dose to patients is also reduced [11–13]. However, most of the currently used bowtie filters are static. Their attenuation profiles are fixed and cannot be adaptively changed by gantry rotation. In recent years, several types of dynamic beam attenuators (DBA) have also been proposed to adapt to radiation exposure more patient-specifically in CT scans [12,14,15], such as wedge-based filters [16–21], sheet-based filters [22–24], bowtie-based transformable filters [25] and fluid-filled filters [26–28]. The fluence modulation can be performed across

beams and projections to provide more homogenous image noise and lower the patient dose [29,30]. However, all filters can only be used in fan-beam CT, and their configurations are relatively complicated. To overcome the above shortcomings, Liu et al. [27] proposed a conceptual design of a fluid dynamic bowtie filter (FDB) for both fan-beam and cone-beam CT (CBCT), which was expected to reduce the patient's dose and improve image quality. The proposed 3D bowtie consists of a highly attenuating bowtie (HB) filled with $CeCl_3$ liquid and a weakly attenuating bowtie (WB) immersed in the liquid. The HB aims at a balanced flux distribution on a detector array when no object is in the field of view (FOV). WB consists of air compensating for an object in the FOV and thus is a scaled-down version of the object. The WB can be rotated and translated synchronously with the source rotation and patient translation. Therefore, the overall flux balance is maintained in the detector array. It was expected that the 3D FDB could more efficiently reduce the patient dose and improve image quality.

In this study, based on the conceptual design of the FDB proposed by Liu et al. [27], a more comprehensive evaluation of dose reduction and image quality of the head, thorax and abdomen CBCT scans was performed using Monte Carlo simulations. The results of this study will be helpful in optimizing the design of FDB and promoting its clinical application.

2. Materials and Methods

2.1. Modeling of a CBCT Scanner with Different Bowties

Figure 1 illustrates the geometry of a CBCT scanner and two different bowties. The cone-beam covers a panel detector with dimensions of 936 × 936 mm^2 (the pitch is 1.0 mm for each pixel), and the source angular aperture is 25°. The source-to-detector distance was 1060 mm, and the source-to-isocenter distance was 570 mm. In this study, two types of bowtie filters were assumed to be used in CBCT. The thicknesses of the FDB and U-type static bowtie filter (SB) made of aluminum were 60 and 45 mm, respectively, and their distances to the source were 114 and 124 mm, respectively. For SB, both head and body bowties made of aluminum were considered. The detailed configuration of the DFB is listed in Table 1.

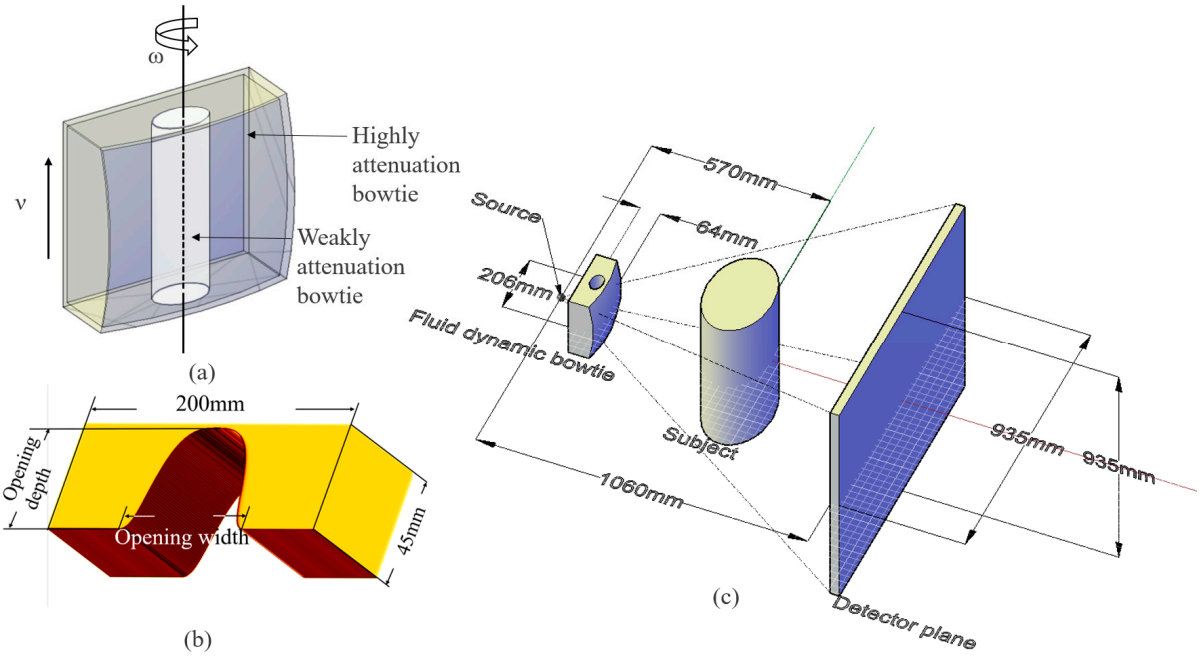


Figure 1. Geometry of the fluid dynamic bowtie (**a**), static bowtie filter (**b**) and a cone-beam CT scanner with a flat panel detector plate (**c**).

Table 1. Material composition inside of the FDB [27].

Item	Material	Density	Size
HB attenuator	$CeCl_3$ solution	1.23 mg/mL	Variable [(a)]
HB container	Aluminum	2.7 mg/mm^3	0.5 mm thickness
WB attenuator	Air	1.29 mg/mm^3	Variable [(a)]
WB container	C-525 plastic	1.29 mg/mm^3	0.2 mm thickness

[(a)] The WB attenuator is an elliptic cylinder, and its size will change with the scanning subject.

To simplify the designs of the WB and the U-shaped SB, the imaging procedures were divided into head, thorax and abdomen examinations; the scanning lengths were set to 300 mm, 400 mm and 400 mm; and the sizes of the three body parts were equivalent to elliptical cylinders according to the reference adult phantom [31]. Based on the geometry of the CBCT shown in Figure 1, the sizes of the WBs in the FDB and the openings of the SB are designed, which are listed in Table 2. It is worth mentioning that only the head and body SB are used in this study, and different openings in the SB are not further considered for the thorax and abdomen imaging.

Table 2. Sizes of WBs in the FDB and openings of the SB that are designed in this study.

Body Part	WB in the FDB (mm)			Opening of the SB (mm)	
	Major Axis	Minor Axis	Length	Width	Depth
Head	40.8	30.4	60.0	76.0	43.0
Thorax	72.0	40.6	80.0	88.0	43.0
Abdomen	62.0	41.6	80.0	88.0	43.0

2.2. Image Reconstruction

In this study, the five imaging tasks shown in Figure 2 were considered. First, head equivalent and body (thorax or abdomen) equivalent elliptical water phantoms were tested, since the designs of WBs in the FDB and U-typed openings in the SB were expected to best fit the elliptical cylinders. Second, typical head, thorax and abdomen scans of an adult were selected to investigate the practical performances of the FDB and SB.

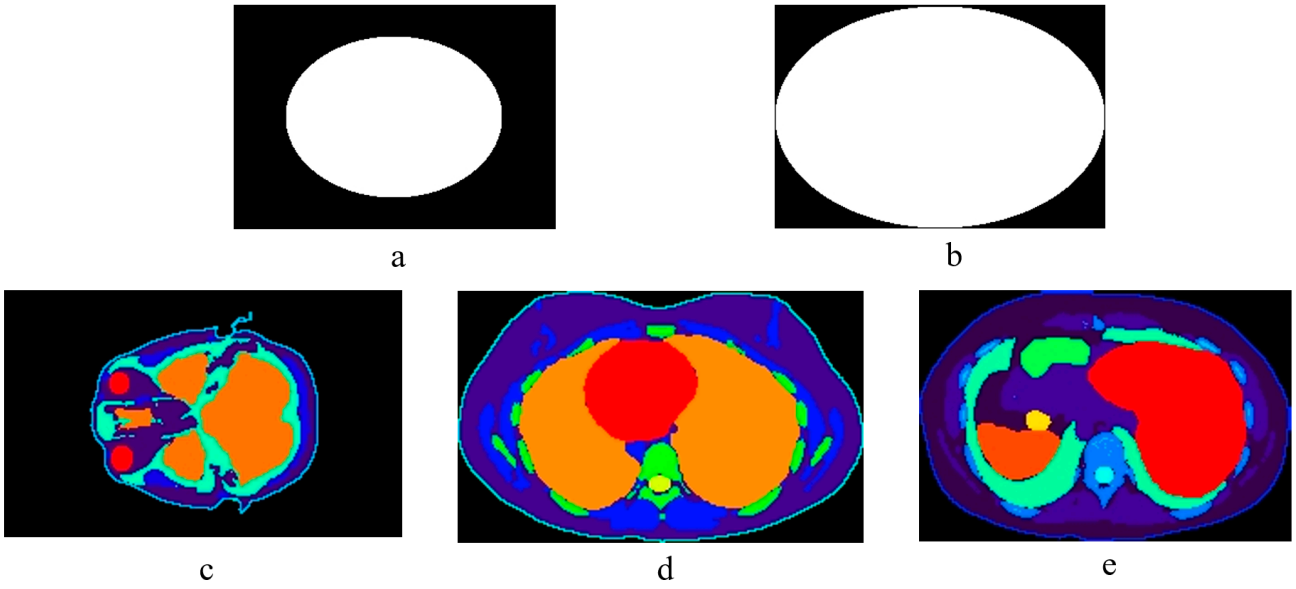


Figure 2. Image tasks considered in this work. (**a**) Head-equivalent water phantom, (**b**) body-equivalent water phantom, (**c**) adult head, (**d**) adult thorax and (**e**) adult abdomen.

For a more accurate simulation of the images, the energy spectrum of the X-ray source was also considered in this work, and it was generated using the software Spektr 3.0 (The I-STAR Lab, Baltimore, MD, USA) [31] at a tube peak voltage of 120 kVp. The photon numbers reaching the detection panel were first calculated by using the Beer–Lambert law [32] in which the radiation attenuation length is calculated based on Siddon's algorithm [33]. Additionally, Poisson noise was further added to the primary signal to acquire the noise-added sinogram and reconstruct the image by using the FDK algorithm [34]. Then, another independent Poisson noise was added again to reconstruct another image to study the image noise. The noise was evaluated based on the different HU values for the same regions of interest (ROIs) in the two images with an index of the inverse of image variance (σ^2) [28,35].

To simulate the images using the angular TCM technique, the product of tube current and exposure time for each projection, denoted as exposure (E), was calculated based on the following algorithm [36].

$$E(p) = E_{\text{ref}}(e^{\alpha(L(p)-L_{\text{ref}})}) \quad (1)$$

where $L(p)$ is the maximum radiological path length in projection p. E_{ref} and L_{ref} are the reference E value and radiological path length, respectively. α was set at 0.5. In general, $L(p)$ can be estimated using the two localizer radiographs and is calculated as follows:

$$L(p) = L_{\text{AP}} + \frac{L_{\text{LAT}} - L_{\text{AP}}}{2}(1 + cos(2\varphi)) \quad (2)$$

where L_{AP} and L_{LAT} are the maximum radiological path lengths for anteroposterior (AP) and lateral (LAT) radiographs, respectively, and φ is the tube angle (φ = 0 corresponds to the lateral view).

For a more comprehensive comparison of the radiation dose and image quality using different attenuators and techniques, six scanning protocols were simulated in this study and are listed in Table 3.

Table 3. Scanning protocols are simulated in this study.

Scanning Protocol	Attenuator	TCM
NoAtt_tcm0	No	Off
SB_tcm0	Static bowtie filter	Off
FDB_tcm0	Fluid dynamic bowtie filter	Off
NoAtt_tcm1	No	On
SB_tcm1	Static bowtie filter	On
FDB_tcm1	Fluid dynamic bowtie filter	On

2.3. Image Quality Calculation

For a more reasonable comparison of the image quality using different scanning protocols, the fluence of each protocol was adjusted so that the image noise of different protocols was normalized to the same as the scanning protocol without any attenuation or current modulation. Then, the noise power spectrum (NPS) or NPS isotropy, which can demonstrate the noise magnitude, texture or spatial resolution directionality, was used as an index to compare the image quality [37]. Through Fourier transformation, the 2D NPS was first calculated for the largest central square region of the same imaging task using different scanning protocols. Then, the radial profile of the NPS was sampled from the 2D NPS at an interval of 1°. The area under the 1D NPS profile at each angle can be calculated as:

$$A(\varphi) = \int_0^\infty NPS_{1\text{D}}(\varphi)kdk \quad (3)$$

where φ is the polar angle, k is the spatial frequency and the NPS is calculated as follows:

$$NPS = \frac{b_x b_y}{L_x L_y}|DFT[g(x,y) - g_{\text{bkg}}(x,y)]|^2 \quad (4)$$

where b_x, b_y are the pixel dimensions, L_x, L_y are the number of ROI voxels in each dimension, *DFT* refers to the discrete Fourier transform and g is the single image acquisition. Then, the NPS score isotropy is estimated as:

$$\varepsilon_{\mathrm{NPS}} = \langle \frac{A(\varphi)}{A_{\max}} \rangle \tag{5}$$

where $A_{\max}$ is the maximum $A(\varphi)$.

2.4. Dose Calculation

For a more reasonable comparison of the radiation doses among the different scanning protocols, the fluence was modulated to maintain the image noise of the different protocols the same as the scanning protocol without any attenuation or current modulation. The radiation doses absorbed in the phantoms and subjects were then simulated using the Monte Carlo method. In the simulations, the physical model of the standard electromagnetic process was selected to simulate photon transport and deposition, and the deposited energy in each voxel size of 2 mm × 2 mm × 2 mm in the phantom or subject was automatically recorded. All simulations were performed using GPU-accelerated Geant4 code [38]. In each simulation, a history of 1×10^8 events was preset, and the uncertainty of dose calculation in each voxel was confirmed to be less than 1%.

3. Results

3.1. Projection Profile and Energy Spectrum

Figure 3 shows the simulated photon counts reaching the detector panel along the anteroposterior (AP) direction of the body-equivalent water phantom and the adult abdomen using different bowtie filters. The photon counts of each channel were further normalized to the photon counts at the boundary of the detector plane where no beam passed through the subject. As shown in Figure 3, compared with using the SB or without any attenuation filter, the modulation of photon numbers among different channels of the detector was the best when using the FDB. This indicates that the FDB can efficiently improve the fluence modulation performance of the CBCT.

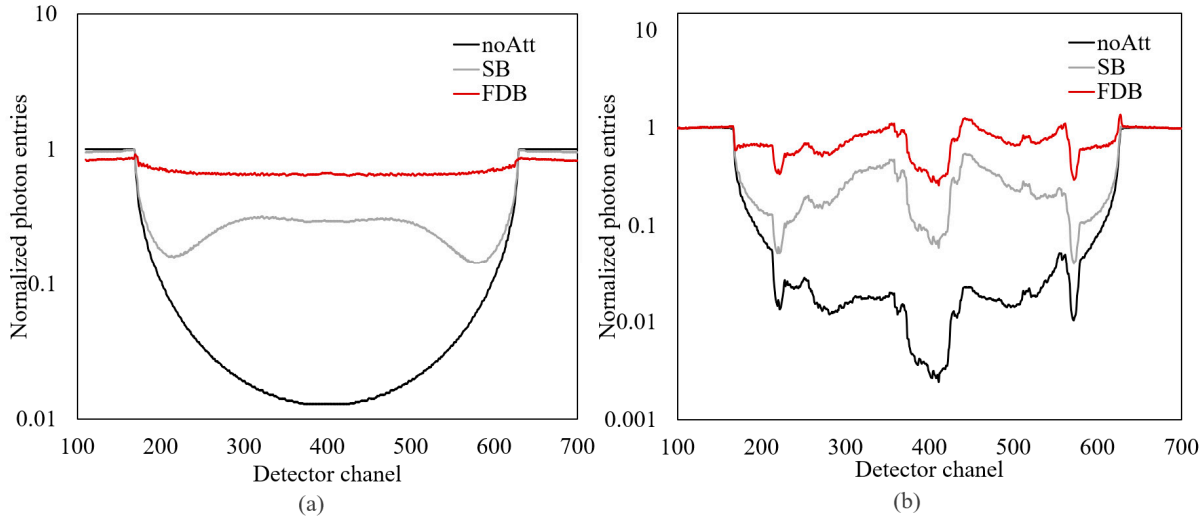


Figure 3. Normalized photon counts reaching the detector panel along the AP direction using different bowties for scanning (**a**) body-equivalent water phantom and (**b**) an adult abdomen.

Figure 4 shows the simulated X-ray energy spectra of the CBCT at the project center using different attenuation filters. First, we used the software of Spektr 3.0 to generate the preliminary spectra of X-ray originating from the CT tube without the bowties. Then, based on the preliminary spectra and configurations of the bowties, the X-ray spectra

of the CBCT were further simulated by using the GGEMs, a GPU Geant4-based Monte Carlo simulation. As shown in Figure 4, SB hardly changed its original energy spectrum; however, FDB significantly changed the original distribution of the energy spectrum, and the average energy was much higher. The result implies that the radiation dose absorbed by the patients and the image quality might change when using FDB.

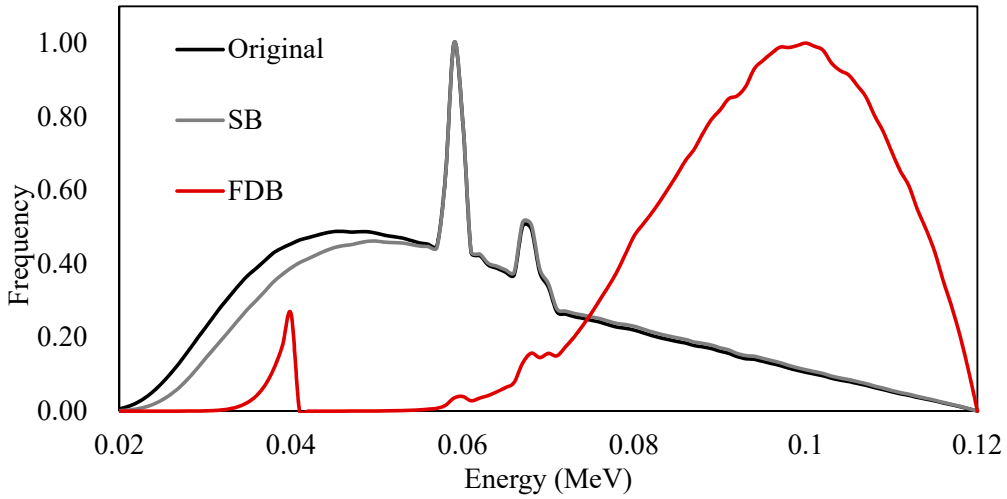


Figure 4. X-ray energy spectra adding different bowties at a tube voltage of 120 kVp.

3.2. Doses Deposited in the Water Phantoms

Figure 5 shows the simulated dose maps in the head equivalent and body-equivalent water phantoms using different scanning protocols; the dose was normalized to the maximum value when neither an attenuation filter nor TCM was used. As shown in Figure 5, using the FDB or SB obviously reduces the dose deposited in the whole head and body-equivalent water phantoms, especially for the surface layer of the phantom. Compared with SB, the dose reduction effect using FDB is more obvious. It is considered that the increase in the effective energy reduces the radiation dose deposited in the surface layer (Figure 4), and the FDB can generate a more constant fluence across the elliptical projections (Figure 3). However, the effect of TCM was less obvious.

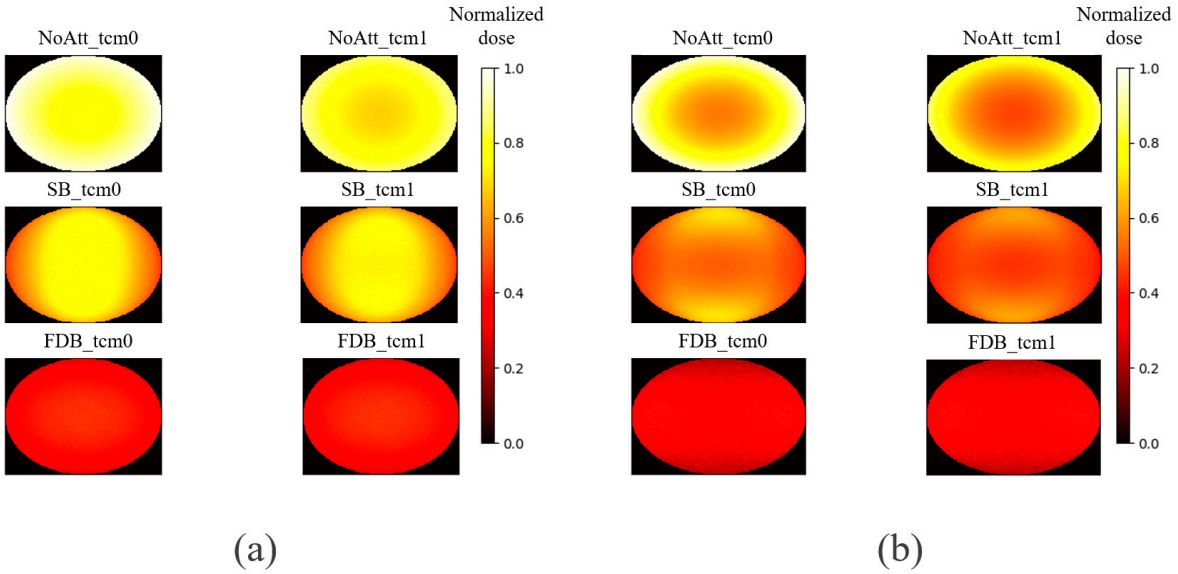


Figure 5. Dose map of (**a**) head and (**b**) body phantom using different scanning protocols.

For quantitative comparison, the doses deposited in all voxels of the phantoms were extracted and averaged. Table 4 summarizes the relative average doses deposited in the head and body phantoms using the different scanning protocols. As shown in Table 4, compared to the NoAtt_tcm0, the doses received by both head and body-equivalent water phantoms were reduced by 57% when the FDB was used, and the doses were also reduced by 23% and 35% for the head and body phantoms using the SB, respectively. The results indicate that FDB can reduce the radiation dose more efficiently than SB.

Table 4. Relative dose deposited in the head and body phantoms using different scanning protocols.

Scanning Protocol	Head Phantom	Body Phantom
NoAtt_tcm0	1	1
SB_tcm0	0.79 (0.44–1.02)	0.73 (0.39–0.95)
FDB_tcm0	0.43 (0.24–0.62)	0.43 (0.17–0.78)
NoAtt_tcm1	0.90 (0.89–0.90)	0.87 (0.85–0.88)
SB_tcm1	0.77 (0.44–0.99)	0.65 (0.38–0.84)
FDB_tcm1	0.43 (0.24–0.62)	0.43 (0.17–0.78)

3.3. Doses Received by the Main Organs Underwent a Typical Head, Thorax and Abdomen Scan

Figure 6 illustrates the simulated dose maps in an adult head, thorax and abdomen using different scanning protocols, and the doses were normalized to their corresponding maximum values when neither attenuation filter nor TCM was used. As shown in Figure 6, both FDB and SB could also reduce the doses absorbed in the adult head, thorax and abdomen.

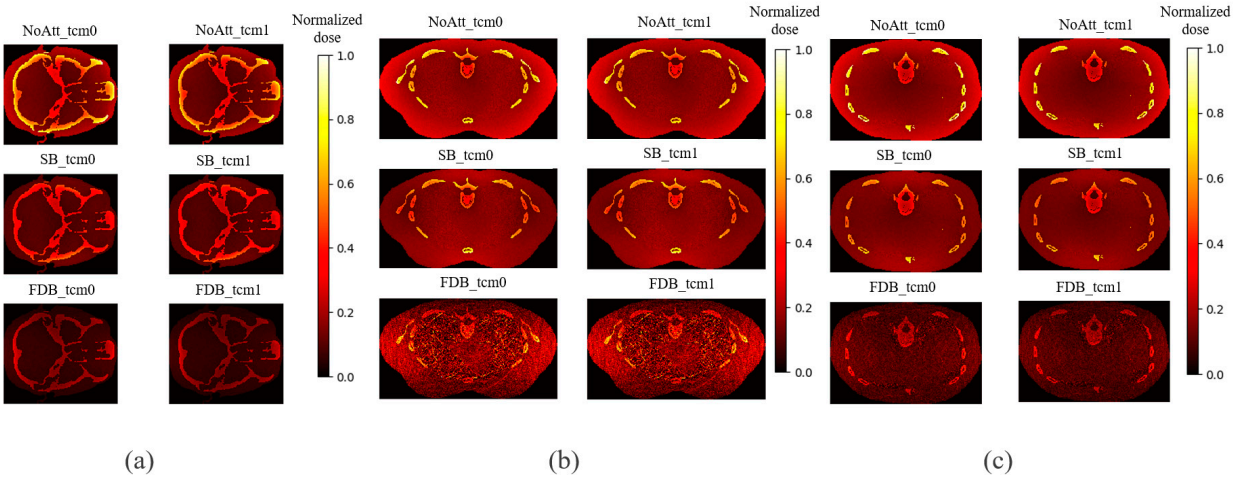


Figure 6. Dose map for adult (**a**) head, (**b**) thorax and (**c**) abdomen scans using different scanning protocols.

For a quantitative comparison, the absorbed doses in all voxels of the three body parts and the main organs were extracted and averaged. Table 5 summarizes the relative total doses and organ doses absorbed in the head, thorax and abdomen using the different scanning protocols. As shown in Table 5, compared with NoAtt_tcm0, the average total doses received by the head, thorax and abdomen were reduced by 70%, 34% and 60%, respectively, using the FDB combined with the TCM technique, and the average total doses received by the head, thorax and abdomen were only reduced by 34%, 16% and 26%, respectively, using the SB combined with the TCM technique. Compared to the dose reductions in the head and body water phantoms (Table 4), it was found that the reduction ratios were even larger in the adult head and abdomen. These results can be explained by the average density of the head and abdomen being higher than that of water, and they absorb relatively lower doses as the X-ray energy increases [39]. Furthermore, as seen in

Table 5, the main organ doses in the head, thorax and abdomen were also most efficiently reduced using the FDB_tcm1 protocol. These results confirm that FDB can also efficiently reduce the radiation dose to patients.

Table 5. The relative dose absorbed in the head, thorax and abdomen using different scanning protocols.

Protocol	Head			Thorax		Abdomen		
	Whole [(a)]	Brain	Eyes	Whole [(a)]	Lungs	Whole [(a)]	Intestine	Stomach
NoAtt_tcm0	1	1	1	1	1	1	1	1
SB_tcm0	0.69	0.80	0.71	0.85	0.94	0.78	0.84	0.85
FDB_tcm0	0.33	0.41	0.43	0.68	0.87	0.43	0.55	0.58
NoAtt_tcm1	0.91	0.91	0.91	0.96	0.97	0.94	0.94	0.94
SB_tcm1	0.66	0.76	0.67	0.84	0.92	0.74	0.81	0.80
FDB_tcm1	0.30	0.37	0.38	0.66	0.85	0.40	0.52	0.54

[(a)] Average of all voxels.

3.4. NPS Isotropy

In this study, the noise uniformity at the center of the subject was used to evaluate image quality. Table 6 summarizes the simulated results of the NPS isotropy for different subjects using different scanning protocols. As shown in Table 6, NPS isotropy can also be improved by using bowties or the TCM technique. For all subjects, the NPS isotropy score was always the best when using the FDB. In adults, the NPS isotropy score was further improved in combination with the TCM technique. This indicates that the FDB can not only reduce the dose for patients, but also improve the image quality during CT scans.

Table 6. NPS isotropy of reconstructed images using different scanning protocols.

Scanning Protocol	Water Phantom		An Adult		
	Head	Body	Head	Thorax	Abdomen
NoAtt_tcm0	0.49	0.31	0.40	0.35	0.45
SB_tcm0	0.59	0.39	0.43	0.35	0.45
FDB_tcm0	0.67	0.51	0.47	0.45	0.59
NoAtt_tcm1	0.59	0.35	0.46	0.38	0.51
SB_tcm1	0.65	0.45	0.46	0.42	0.55
FDB_tcm1	0.67	0.51	0.51	0.46	0.64

4. Discussion

In this study, based on the conceptual design of the FDB proposed by Liu et al. [27], more comprehensive evaluations of dose reduction and image quality of the head, thorax and abdomen scans were carried out through theoretical studies. In calculating the radiation dose, the Monte Carlo method, which is considered the gold standard for dose calculation, was used [40–43], and the energy distribution of X-rays was also considered. The results show that the energy spectra of the X-rays change with the type of attenuation filter (bowties). Therefore, the relative dose calculated in this study was considered to be more accurate. Furthermore, we investigated the radiation dose and image quality using different scanning protocols based on the same specified image noise. Therefore, the comparisons are considered to be more reasonable.

According to the preliminary results of this study, it is confirmed that FDB has a greater potential to reduce the radiation dose to the patient and improve the image quality than SB, regardless of the scanning parts of the patients. Especially for the organs or tissues in the surface layer of patients, the absorbed doses can be significantly reduced using FDB. The main reason for this is that the WB in the FDB is three-dimensional and dynamic, and it is easy adjust to match the scanned subject.

However, more studies and developments are needed to put FDB into clinical use. First, a technique for controlling the changes in the weakly attenuating bowtie (WB) in volume, shape and position to match the scanning parts of individual patients must be developed. The optimal liquid component used as the HB is also worth investigating. Furthermore, only the CBCT was studied in this work, and further studies on fan-beam CT might be more useful.

5. Conclusions

The FDB, consisting of a highly attenuating bowtie and a weakly attenuating bowtie, has greater potential to reduce the dose to the patient than that of the currently available SB, regardless of the scanning parts of the patient. Especially for the organs or tissues in the surface layer of patients, the absorbed doses can be largely reduced using the FDB. Furthermore, FDB combined with the TCM technique can also improve the NPS isotropy of reconstructed images, which is helpful for disease diagnoses. Further works are worth conducting to integrate the FDB into clinical uses.

Author Contributions: Methodology, X.L., W.Z.; software, X.L.; validation, X.L., W.Z.; analysis, W.Z., X.L.; investigation, X.L., W.Z.; writing—original draft preparation, W.Z., X.L.; writing—review and editing, X.L., W.Z., H.L., T.X.; visualization, X.L.; funding acquisition, H.L., W.Z. All authors have read and agreed to the published version of the manuscript.

Funding: This work was partially supported by the National Natural Science Foundation of China (Nos. 12175043, 12075064).

Institutional Review Board Statement: Not applicable.

Informed Consent Statement: Not applicable.

Conflicts of Interest: The authors declare no conflict of interest.

References

1. United Nations Scientific Committee on the Effects of Atomic Radiation. *Sources, Effects and Risks of Ionizing Radiation UNSCEAR 2020/2021 Report*; United Nations Scientific Committee on the Effects of Atomic Radiation: Vienna, Austria, 2022.
2. Brenner, D.J.; Elliston, C.D.; Hall, E.J.; Berdon, W.E. Estimated risks of radiation-induced fatal cancer from pediatric CT. *Am. J. Roentgenol.* **2001**, *176*, 289–296. [CrossRef] [PubMed]
3. Brenner, D.J. Estimating cancer risks from pediatric CT: Going from the qualitative to the quantitative. *Pediatric Radiol.* **2002**, *32*, 228–231. [CrossRef]
4. Sodickson, A.; Baeyens, P.F.; Andriole, K.P.; Prevedello, L.M.; Nawfel, R.D.; Hanson, R.; Khorasani, R. Recurrent CT, Cumulative Radiation Exposure, and Associated Radiation-induced Cancer Risks from CT of Adults. *Radiology* **2009**, *251*, 175–184. [CrossRef] [PubMed]
5. McCollough, C.H.; Primak, A.N.; Braun, N.; Kofler, J.; Yu, L.; Christner, J. Strategies for reducing radiation dose in CT. *Radiol. Clin.* **2009**, *47*, 27–40. [CrossRef] [PubMed]
6. Gies, M.; Kalender, W.A.; Wolf, H.; Suess, C.; Madsen, M.T. Dose reduction in CT by anatomically adapted tube current modulation. I. Simulation studies. *Med. Phys.* **1999**, *26*, 2235–2247. [CrossRef]
7. Kalender, W.A.; Wolf, H.; Suess, C. Dose reduction in CT by anatomically adapted tube current modulation. II. Phantom measurements. *Med. Phys.* **1999**, *26*, 2248–2253. [CrossRef]
8. Kalender, W.A.; Wolf, H.; Suess, C.; Gies, M.; Greess, H.; Bautz, W.A. Dose reduction in CT by on-line tube current control: Principles and validation on phantoms and cadavers. *Eur. Radiol.* **1999**, *9*, 323–328. [CrossRef]
9. Kopka, L.; Funke, M.; Breiter, N.; Hermann, K.P.; Vosshenrich, R.; Grabbe, E. An anatomically adapted variation of the tube current in CT. Studies on radiation dosage reduction and image quality. *Rofo* **1995**, *163*, 383–387. [CrossRef]
10. Christner, J.A.; Zavaletta, V.A.; Eusemann, C.D.; Walz-Flannigan, A.I.; McCollough, C.H. Dose reduction in helical CT: Dynamically adjustable z-axis X-ray beam collimation. *Am. J.Roentgenol.* **2010**, *194*, W49–W55. [CrossRef]
11. Bootsma, G.J.; Verhaegen, F.; Jaffray, D.A. The effects of compensator and imaging geometry on the distribution of X-ray scatter in CBCT. *Med. Phys.* **2011**, *38*, 897–914. [CrossRef]
12. Graham, S.A.; Moseley, D.J.; Siewerdsen, J.H.; Jaffray, D.A. Compensators for dose and scatter management in cone-beam computed tomography. *Med. Phys.* **2007**, *34*, 2691–2703. [CrossRef] [PubMed]
13. Mail, N.; Moseley, D.J.; Siewerdsen, J.H.; Jaffray, D.A. The influence of bowtie filtration on cone-beam CT image quality. *Med. Phys.* **2009**, *36*, 22–32. [CrossRef] [PubMed]

14. Hsieh, J. Adaptive streak artifact reduction in computed tomography resulting from excessive X-ray photon noise. *Med. Phys.* **1998**, *25*, 2139–2147. [CrossRef]
15. Stiller, W.; Veloza, S.; Kauczor, H. Attenuation-based dynamic CT beam-shaping filtration in dependence of fan and projection angle: Evaluation of a new method for radiation exposure reduction by Monte-Carlo simulation of spatial dose distribution. In Proceedings of the 2012 IEEE Nuclear Science Symposium and Medical Imaging Conference Record (NSS/MIC), Anaheim, CA, USA, 27 October–3 November 2012; pp. 2625–2632.
16. Hsieh, S.S.; Pelc, N.J. The feasibility of a piecewise-linear dynamic bowtie filter. *Med. Phys.* **2013**, *40*, 031910. [CrossRef] [PubMed]
17. Hsieh, S.S.; Peng, M.V.; May, C.A.; Shunhavanich, P.; Fleischmann, D.; Pelc, N.J. A prototype piecewise-linear dynamic attenuator. *Phys. Med. Biol.* **2016**, *61*, 4974–4988. [CrossRef]
18. Szczykutowicz, T.P.; Hermus, J.; Geurts, M.; Smilowitz, J. Realization of fluence field modulated CT on a clinical TomoTherapy megavoltage CT system. *Phys. Med. Biol.* **2015**, *60*, 7245–7257. [CrossRef]
19. Szczykutowicz, T.P.; Mistretta, C.A. Design of a digital beam attenuation system for computed tomography. Part II. Performance study and initial results. *Med. Phys.* **2013**, *40*, 021906. [CrossRef]
20. Szczykutowicz, T.P.; Mistretta, C.A. Design of a digital beam attenuation system for computed tomography: Part I. System design and simulation framework. *Med. Phys.* **2013**, *40*, 021905. [CrossRef]
21. Szczykutowicz, T.P.; Mistretta, C.A. Experimental realization of fluence field modulated CT using digital beam attenuation. *Phys. Med. Biol.* **2014**, *59*, 1305–1326. [CrossRef]
22. Huck, S.M.; Fung, G.S.K.; Parodi, K.; Stierstorfer, K. Technical Note: Sheet-based dynamic beam attenuator—A novel concept for dynamic fluence field modulation in X-ray CT. *Med. Phys.* **2019**, *46*, 5528–5537. [CrossRef]
23. Huck, S.M.; Fung, G.S.K.; Parodi, K.; Stierstorfer, K. The z-sbDBA, a new concept for a dynamic sheet-based fluence field modulator in X-ray CT. *Med. Phys.* **2020**, *47*, 4827–4837. [CrossRef] [PubMed]
24. Huck, S.M.; Fung, G.S.K.; Parodi, K.; Stierstorfer, K. On the potential of ROI imaging in X-ray CT—A comparison of novel dynamic beam attenuators with current technology. *Med. Phys.* **2021**, *48*, 3479–3499. [CrossRef] [PubMed]
25. Liu, F.; Wang, G.; Cong, W.; Hsieh, S.S.; Pelc, N.J. Dynamic bowtie for fan-beam CT. *J. X-ray Sci. Technol.* **2013**, *21*, 579–590. [CrossRef] [PubMed]
26. Hermus, J.R.; Szczykutowicz, T.P. Two-dimensional dynamic fluid bowtie attenuators. *J. Med. Imaging* **2016**, *3*, 013502. [CrossRef]
27. Liu, F.; Yang, Q.; Cong, W.; Wang, G. Dynamic bowtie filter for cone-beam/multi-slice CT. *PLoS ONE* **2014**, *9*, e103054. [CrossRef]
28. Shunhavanich, P.; Hsieh, S.S.; Pelc, N.J. Fluid-filled dynamic bowtie filter: Description and comparison with other modulators. *Med. Phys.* **2019**, *46*, 127–139. [CrossRef]
29. Bartolac, S. Compensator models for fluence field modulated computed tomography. *Med. Phys.* **2013**, *40*, 121909. [CrossRef]
30. Bartolac, S.; Graham, S.; Siewerdsen, J.; Jaffray, D. Fluence field optimization for noise and dose objectives in CT. *Med. Phys.* **2011**, *38* (Suppl. S1), S2–S17. [CrossRef]
31. Punnoose, J.; Xu, J.; Sisniega, A.; Zbijewski, W.; Siewerdsen, J.H. Technical Note: Spektr 3.0—A computational tool for X-ray spectrum modeling and analysis. *Med. Phys.* **2016**, *43*, 4711–4717. [CrossRef]
32. Fuwa, K.; Vallee, B.L. Physical basis of analytical atomic absorption spectrometry—Pertinence of beer-lambert law. *Anal. Chem.* **1963**, *35*, 942–946. [CrossRef]
33. Sundermann, E.; Jacobs, F.; Christiaens, M.; De Sutter, B.; Lemahieu, I. A Fast Algorithm to Calculate the Exact Radiological Path through a Pixel Or Voxel Space. *J. Comput. Inf. Sci. Eng.* **1998**, *6*, 89–94.
34. Rodet, T.; Noo, F.; Defrise, M. The cone-beam algorithm of Feldkamp, Davis, and Kress preserves oblique line integrals. *Med. Phys.* **2004**, *31*, 1972–1975. [CrossRef] [PubMed]
35. Hsieh, S.S.; Pelc, N.J. Control algorithms for dynamic attenuators. *Med. Phys.* **2014**, *41*, 061907. [CrossRef] [PubMed]
36. Jadick, G.; Abadi, E.; Harrawood, B.; Sharma, S.; Segars, W.P.; Samei, E. A framework to simulate CT images with tube current modulation. In *Medical Imaging 2021: Physics of Medical Imaging*; SPIE: Bellingham, WA, USA, 2021; Volume 11595, pp. 22–30.
37. Gang, G.J.; Stayman, J.W.; Zbijewski, W.; Siewerdsen, J.H. Task-based detectability in CT image reconstruction by filtered backprojection and penalized likelihood estimation. *Med. Phys.* **2014**, *41*, 081902. [CrossRef]
38. Lemaréchal, Y.; Bert, J.; Falconnet, C.; Després, P.; Valeri, A.; Schick, U.; Pradier, O.; Garcia, M.P.; Boussion, N.; Visvikis, D. GGEMS-Brachy: GPU GEant4-based Monte Carlo simulation for brachytherapy applications. *Phys. Med. Biol.* **2015**, *60*, 4987–5006. [CrossRef] [PubMed]
39. Hubbell, J.H. Tables of X-ray Mass Attenuation Coefficients and Mass Energy-Absorption Coefficients (Version 1.4). 2004. Available online: http://physics.nist.gov/xaamdi (accessed on 15 March 2022).
40. Harki, E.M.T.; Al-Kinani, A.T. Measurement of organ dose in chest CT examination using Monte Carlo simulation. *Iran. J. Radiat. Res.* **2007**, *4*, 205–209.
41. Chang, K.-H.; Lee, W.; Choo, D.-M.; Lee, C.-S.; Kim, Y. Dose reduction in CT using bismuth shielding: Measurements and Monte Carlo simulations. *Radiat. Prot. Dosim.* **2010**, *138*, 382–388. [CrossRef]
42. Gao, Y.; Ding, A.; Zhang, D.; Liu, B.; Caracappa, P. Monte Carlo Simulation and Dose Calculation of Chest CT Scan with Tube Current Modulation. *Med. Phys.* **2013**, *40*, 458. [CrossRef]
43. Liu, T.; Du, X.; Su, L.; Gao, Y.; Ji, W.; Zhang, D.; Shi, J.; Liu, B.; Kalra, M.; Xu, X. Monte Carlo CT Dose Calculation: A Comparison Between Experiment and Simulation Using ARCHER-CT. *Med. Phys.* **2014**, *41*, 424. [CrossRef]